Title	Morphology, structure and electrochemical properties of single phase electrospun vanadium pentoxide nanofibers for lithium ion batteries
Author(s)	Cheah, Yan Ling; Gupta, Nutan; Pramana, Stevin S.; Aravindan, Vanchiappan; Wee, Grace; Srinivasan, Madhavi
Citation	Cheah, Y. L., Gupta, N., Pramana, S. S., Aravindan, V., Wee, G., & Srinivasan, M. (2011). Morphology, Structure and Electrochemical Properties of Single Phase Electrospun Vanadium Pentoxide Nanofibers for Lithium Ion Batteries. Journal of Power Sources, 196, 6465-6472.
Date	2011
URL	http://hdl.handle.net/10220/7028
Rights	© 2011 Elsevier. This is the author created version of a work that has been peer reviewed and accepted for publication by Journal of Power Sources, Elsevier. It incorporates referee's comments but changes resulting from the publishing process, such as copyediting, structural formatting, may not be reflected in this document. The published version is available at: http://dx.doi.org/10.1016/j.jpowsour.2011.03.039.

Morphology, structure and electrochemical properties of single phase electrospun vanadium pentoxide nanofibers for lithium ion batteries

Yan L. Cheah[a], Nutan Gupta[a], Stevin S. Pramana[b], Vanchiappan Aravindan[b], Grace Wee[a], Madhavi Srinivasan[a,]*

[a] *School of Materials Science and Engineering, Nanyang Technological University, Singapore 639798, Singapore*

[b] *Energy Research Institute, Nanyang Technological University, 50 Nanyang Drive, Singapore 637553, Singapore*

**Corresponding author. Tel.: +65 6790 4606; fax: +65 6790 9081.*

E-mail address: Madhavi@ntu.edu.sg (M. Srinivasan).

ABSTRACT

One-dimensional (1D) vanadium pentoxide (V_2O_5) nanofibers (VNF) are synthesized by electrospinning vanadium sol–gel precursors containing vanadyl acetylacetonate and poly(vinylpyrrolidone) followed by sintering. Crystal structure, molecular structure and morphology of electrospun VNF are analyzed using field emission scanning electron microscopy (FESEM), transmission electron microscopy (TEM), selected area diffraction (SAED), X-ray diffraction (XRD) and Fourier transform infrared spectroscopy (FT-IR). Single-phase electrospun VNF ~300–800 nm in diameter, 20–50μm long (aspect ratio >50) with porous interconnected fibrous morphology are revealed by FESEM and TEM analysis. Electrochemical properties of the sintered VNF, as a cathode in lithium-ion batteries, explored using cyclic voltammetry (CV), galvanostatic charge/discharge and electrochemical impedance spectroscopy (EIS) give rise to new understandings of the electrochemical processes occurring in these nanofibrous cathodes. Electrospun VNF exhibits initial discharge capacity ~316mAhg^{-1} (~2.2 Li per V_2O_5) in the voltage range of

1.75 and 4.0 V vs. Li/Li^+ at 0.1 C rate. When cycled at a reduced voltage range of 2.0–4.0 V vs. Li/Li^+, less phase transitions occur, giving rise to the initial specific capacity of 308 mAh g^{-1} and improved cyclic retention of 74% after 50 cycles.

Keywords

Vanadium pentoxide, Electrospinning, Lithium ion batteries, Nanofibers

1. INTRODUCTION

Lithium ion batteries (LIB) are promising energy storage technologies for electric vehicle (EV), hybrid and plug-in hybrid (HEV/P-HEV) applications. State of art cathode ($LiCoO_2$) used in LIB for portable electronic devices have a maximum capacity of only ~140 mAh g^{-1}. Other cathode chemistries such as olivine ($LiFePO_4$), spinel ($LiMn_2O_4$) and $LiNi_{1/3}Mn_{1/3}Co_{1/3}O_2$ possess advantages over $LiCoO_2$ but still deliver capacities in the range of 100–170 mAh g^{-1} leading to LIB specific energy densities of ~200 W h kg^{-1}. In order to provide for future large scale EV and renewable energy storage applications, there is a pressing need for high energy density LIBs (>1000 W h kg^{-1}) and the bulk of the energy density in LIBs is contributed by the cathode. Hence, there is a need for alternative high capacity cathode insertion materials that exhibit much higher energy densities than the current cathodes. Vanadium based layered oxides with tunable oxidation states (V^{5+}, V^{4+} and V^{3+}) such as VO_2, V_6O_{13} and V_2O_5 are potential cathode materials for rechargeable lithium batteries [1,2]. Among these vanadium pentoxide(V_2O_5) is an attractive candidate for cathodes in Li-ion batteries as they exhibit high theoretical capacities (~400 mAh g^{-1}) due to their capability to intercalate nearly 3 Li^+ ions per mole of active material ($V_2O_5 + xLi^+ + xe^- \leftrightarrow Li_xV_2O_5$) [2].

On the other hand, performance of conventional bulk V_2O_5 powder cathodes is limited by slow lithium diffusion rate ($D \sim 10^{-12}$ cm^2 s^{-1}) in the lattice, structural instability with lithium intercalation/de-intercalation and low electronic conductivity (10^{-2}–10^{-3} S cm^{-1}), leading to inferior battery performance such as low initial capacity, rapid capacity fading

and poor rate capability. In order to improve the electrochemical performance of V_2O_5, there has been an increased interest in fabricating nanoarchitectures of V_2O_5 including hydrothermal process [1], nanowires [1,2], nanorods [3], and nanobelts [4–7] by various methods including sol–gel [8,9], reverse micelle technique [10], and electrodeposition [11,12]. Studies have shown that nanostructured V_2O_5 exhibits better electrochemical performance as compared to bulk V_2O_5 owing to their small particle size, microstructure/morphology that shorten Li-diffusion pathways [13].

Electrospinning is a simple, cost-effective method that enables the synthesis of nanofibers with diameters ranging from tens of nanometers to several micrometers and a large surface area-to-volume ratio [4,5,13–15]. In electrospinning, high accelerating voltage is applied to a needle connected to a syringe containing a sol–gel polymeric precursor. The large electric field, formed between the metallic needle and collector, breaks the surface tension of the polymeric precursor, allowing fibers to form with the continuous evaporation of the solvent upon contact with the ambient atmosphere. Furthermore surface morphology and diameter of the fibers can be easily controlled by varying the electrospinning parameters such as the applied potential, viscosity and flow rate of the precursor. For lithium ion batteries, the key advantage of electrospinning is that it produces macroporous interconnected nanoparticle network of high aspect ratio nanofibers that would provide higher electrode/electrolyte contact surface, better electronic and ionic conductivity and a facile diffusion pathway. Earlier Ban et al. [4,5] fabricated nano δ-V_2O_5 by a two step electrospinning and hydrothermal synthesis method via single crystalline $H_xV_4O_{10}$ $n$$H_2O$ using poly(methyl methacrylate) (PMMA) as the polymeric precursor which resulted in broken nanofibers. Stability in cyclic retention was obtained by intercalation of hydronium (H_3O^+) ions into the V_4H_{10} layers of such fibers. Recently, Mai et al. [16] synthesized multi-phase polycrystalline V_2O_5 nanowires with additional impurities such as V_xO_2 that resulted in additional plateaus during Li intercalation/de-intercalation in the charge and discharge cycles owing to additional phase transformations. To the best of our knowledge, single-phase electrospun V_2O_5 nanofibers for applications in lithium ion batteries have not been synthesized.

Herein, we have fabricated single-phase polycrystalline high aspect ratio V_2O_5 nanofibers (VNF, ~500–800 nm in diameter and 20–50 μm long; aspect ratio >50) by simple one-step electrospinning process using V_2O_5 precursor consisting of vanadium vanadyl acetylacetonate and poly(vinylpyrrolidone), followed by sintering at 400°C for 15min. Electrochemical lithium intercalation studies of electrospun VNF cathodes have been evaluated in half cell configuration (vs. Li) using cyclic voltammetry (CV), galvanostatic charge/discharge and electrochemical impedance spectroscopy (EIS). It was observed that the high purity VNF showed initial discharge capacity ~320mAh g^{-1} and excellent columbic efficiency.

2. EXPERIMENTAL

2.1. Synthesis and characterization of VNF

Poly (vinylpyrrolidone) (PVP, Mw 360,000, Fluka), vanadyl acetylacetonate ($VO(acac)_3$, 98%, Sigma–Aldrich), and acetic acid (Tedia Company Inc.) were mixed in absolute ethanol (Fluka) solvent for 12 h. The well-mixed precursor was electrospun using DC voltage of 10 kV applied between the needle tip and the aluminium foil collector, with a distance of 10 cm, at a flow rate of 2 ml h^{-1}. As-spun fibers [17] were then sintered at 400°C for 15 min, with a heating and cooling rate of 2 °C min^{-1}. Morphology of as-spun and sintered VNF were studied using field emission scanning electron microscope (FESEM, JEOL JSM-7600F) at an accelerating voltage of 5 kV and a transmission electron microscope (TEM, JEOL 2100F) in high resolution mode operating at 200 kV. Multislice simulation was performed using JEMS (Version 3.3111 U2008, P. Stadelmann, CIME-EPFL, Switzerland) for comparison with the high resolution image. Crystal structure of the sintered VNF was examined by Shimadzu X-ray diffractometer (Cu-Kα) with step scanning (0.02°, 0.6s dwell time, 40 kV) over a 2θ range of 10–70°. The obtained X-ray diffraction (XRD) patterns were analyzed by Rietveld refinement [18,19] within the software Topas V3 (Bruker-AXS), using fundamental parameters approach [20]. Fourier transform infrared spectroscopy(FTIR) were recorded on KBr pellets of as-spun and sintered VNF using a Perkin Elmer Spectrum GX FTIR in the range of 4000-400cm^{-1} (step size 2 cm^{-1}).

2.2. Fabrication of electrodes

VNF cathodes were prepared by mixing sintered VNF, Poly (vinylidene fluoride) (PVdF, Sigma–Aldrich), and Super P Li carbon (Timcal) in the weight ratio 60:20:20 respectively in N-methylpyrrolidone (NMP, Sigma–Aldrich) solvent. The viscous slurry was stirred thoroughly and subsequently coated on aluminium foil (Hohsen Corporation) using a doctor blade. Electrodes were dried in a vacuum oven for several hours before compaction. Circular discs (16mm diameter) of both dried VNF electrodes and lithium foil (~0.59 mm thick, Hohsen Corporation, Japan) were punched and used to study the lithium intercalation properties. All the electrochemical studies were carried out using CR 2016 coin cells assembled in an Argon-filled glovebox (MBraun) with metallic lithium in 1 M $LiPF_6$ in ethylene carbonate (EC):diethyl carbonate (DEC) (1:1 v/v) electrolyte and separated by Celgard 2400. Galvanostatic discharge–charge cycling was carried out using battery tester systems (Neware) at room temperature. Cyclic voltammetry (CV) and electrochemical impedance spectroscopy (EIS) were carried out with Solartron, 1470E and SI 1255B Impedance/gain-phase analyzer coupled with a potentiostat. EIS studies were carried out applying amplitude of 10 mV ac voltage over the frequency range of 100 kHz–10 mHz at open circuit potential, before and after cycling at room temperature. The Nyquist plots -Z" vs. Z' were derived and analyzed using Zplot and Zview software (Version 2.2, Scribner Associates Inc., USA).

3. RESULTS AND DISCUSSION

3.1. Morphological and compositional studies

Scanning electron micrographs (Fig. 1a) show nanofibers of as-spun VNF that are 20–60 μm long, 500–1200 nm in diameter with aspect ratio >50. Subsequent sintering of these fibers at 400°C ($2^{\circ}C\ min^{-1}$) led to crystallization of V_2O_5 nanocrystallites (~70–80 nm) and removal of polymer precursor, resulting in a porous nano-particulate interconnected fibrous morphology (Fig. 1b). It is observed that sintered VNF have diameter in the range of 300–800 nm owing to the thermal decomposition of PVP

polymer that resulted in slight fiber shrinkage.

Bright-field TEM images, together with the selected area diffraction (SAED) (Fig. 1c and d) of the VNF clearly show a transition from smooth, amorphous as-spun nanofibers to porous polycrystalline nanofibers after sintering. Sintered VNF are composed of uniformly sized fibers with porous structure, which exhibits polycrystallinity in random orientation with an average crystallite size ~70–80 nm. The selected area electron diffraction (SAED) of the sintered VNF (Fig. 1d inset) shows the random orientation of nanocrystals, consistent with the XRD data of VNF (Fig. 2a), which does not show any preferred orientation. The diffraction rings can be indexed to the (200), (101), (110) and (111) planes of the Shcherbinaite V_2O_5 phase.

High resolution image (Fig. 1e) and SAED of a single VNF nanocrystal (Fig. 1e inset) oriented along [1 3 3] zone axis are obtained and resembles the structure obtained from the simulation (Fig. 1f). The d_{hkl}, calculated from SAED pattern, agree reasonably with the XRD data of VNF sintered at 400 °C. By comparison with the multislice simulation, no defect is observed in the high resolution image, and the thickness of the crystal is estimated to be ~10(2) nm.

Powder X-ray diffraction pattern of sintered VNF (Fig. 2a) collected to elucidate its crystal structure shows the formation of single phase orthorhombic V_2O_5 corresponding to the layered Shcherbinaite structure ($Pmn2_1$) in VNF (Fig. 2b). Rietveld crystal structure analysis using TOPAS software evaluated lattice parameters a = 11.5214(1) Å, b = 4.3738(6) Å, c = 3.5667(4) Å and crystallite size of 78 nm (R_{Bragg} = 5.6) from Scherrer equation. Insertion of lithium atoms into V_2O_5 results in the phase transformation of V_2O_5 to $Li_xV_2O_5$ leading to distortion of the layered structure (Fig. 2b) due to the intercalation of lithium atoms into the spaces between the layers of VO_5 octahedra which will be discussed in the later sections.

FTIR spectra of as-spun and sintered VNF are studied (Fig. 3). Several additional peaks due to the organics are observed in the spectra of the as-spun VNF as comparison to the

sintered VNF. The FTIR bands observed at 3485 and 1642 cm^{-1} for as-spun VNF correspond to O–H stretching and bending modes [4,21,22], which are correlated to the organic solvents ethanol and acetic acid. The peaks at 2946 and 1282 cm^{-1} are due to C–H stretching and bending modes observed due to the presence of PVP in as-spun VNF [23]. The band at 990 cm^{-1} is related to the V=O stretching vibrations [22]. Vibrational modes of O–H and C–H from PVP are absent in the sintered VNF IR spectra, indicating the complete degradation of PVP during the sintering step of VNF. For the spectra of sintered VNF, the peaks around 1026 and 834 cm^{-1} correspond to the V=O stretching vibration and asymmetric stretching of the V–O–V bond respectively. The 637 and 476 cm^{-1} peak in the spectra for sintered VNF correspond to the symmetric stretching of the V–O–V bond [7,22].

The possible mechanism behind the formation of these high-purity VNF is suggested in the schematic shown in Fig. 4. The vanadium-containing precursor $VO(acac)_3$ is dissolved in a solution of ethanol and acetic acid, with addition of PVP to increase the viscosity of the solution. During the electrospinning process, the PVP forms a polymeric scaffold in which the droplets of dissolved $VO(acac)_3$ are evenly dispersed. This enables the formation of a random network of as-spun fibers, as observed under the FESEM (Fig. 1a). Upon sintering, the degradation of PVP and the growth of the V_2O_5 nanoparticles, via the oxidation of $VO(acac)_3$, occur simultaneously. In order to maintain the fibrous morphology of the VNF, a slow rate of temperature increase (2 $^{\circ}C\ min^{-1}$) is required. The sintering process has an annealing effect on the V_2O_5 nanoparticles and allows the nanoparticles to join together, forming porous nanofibers. In addition, the slow sintering rate enables sufficient time for the PVP to be totally degraded, as proven by the FTIR studies (Fig. 3). Formation of such nanofibers with large aspect ratios prevents the agglomeration of nanoparticles.

3.2. Electrochemical studies

Cyclic voltammograms of VNF cells are collected in the range of 1.75–4.0 V vs. Li/Li^+ at a rate of 0.1 mV s^{-1} to study the phase transformation that occurs during lithium intercalation/de-intercalation (cycling) in to V_2O_5.

$$V_2O_5 + xLi^+ + xe^- \leftrightarrow Li_xV_2O_5 \quad (1)$$

During the 1st cycle (Fig. 5a), several oxidation/reduction peaks are observed, corresponding to the intercalation/de-intercalation processes of Li^+ in the VNF. The reduction (cathodic) peaks are observed at 3.16, 2.22, 2.11 and 1.95 V, while one main oxidation current peak is observed at 2.70 V vs. Li/Li^+. The presence of these peaks indicates that the reduction of V^{5+} in V_2O_5 takes place as a multistep process within the voltage range 1.75–4.0 V. The reduction peak at 3.16 V indicates the reduction of V^{5+} to V^{4+}, leading to the formation of ε-$Li_xV_2O_5$, as indicated in Eq. (2) below. At the reduction peaks of 2.22 and 2.11 V, partial reduction of V^{4+} to V^{3+} occurs, leading to the formation of a mixed phase of δ- and γ-$Li_xV_2O_5$, as shown in Eqs. (3) and (4). Upon cycling below 2.0 V vs. Li/Li^+, the γ-$Li_xV_2O_5$ phase (Fig. 2b) is irreversibly formed, as shown by the reduction peak at 1.95 V. This reduction process of the vanadium ion enables the accommodation of more than 2 Li per V_2O_5. Some reverse reactions take place as indicated by the oxidation peak at 2.70 V.

$$\alpha\text{-}V_2O_5 + 0.5Li^+ + 0.5e^- \leftrightarrow \varepsilon\text{-}Li_{0.5}V_2O_5 \quad (2)$$

$$\varepsilon\text{-}Li_{0.5}V_2O_5 + 0.5Li^+ + 0.5e^- \leftrightarrow \delta\text{-}LiV_2O_5 \quad (3)$$

$$\delta\text{-}LiV_2O_5 + Li^+ + e^- \leftrightarrow \gamma\text{-}Li_2V_2O_5 \quad (4)$$

During subsequent cycles (Fig. 5b), only one main oxidation/reduction pair of peaks is present. The reduction peak shifted to 2.27 V, while oxidation peak remained at around 2.68 V. These peaks are intact upon further cycling, indicating the reversibility of oxidation/reduction reactions.

VNF coin cells are cycled between 1.75 and 4.0 V vs. Li/Li^+ at a rate of 0.1 C (or 35 mA

g^{-1}). The first discharge (Fig. 6a) shows multiple plateaus, similar to the data in the work of Ban et al. [4] and Mai et al. [16]. Due to the absence of impurities in VNF, additional plateaus at 2.8 and 2.5 V, attributed to the V_xO_2 impurities by Mai et al.[16], are not observed. The first discharge plateau occurs at 3.18 V vs. Li/Li^+, this can be correlated to the reduction peak occurring at 3.16 V, indicating the reduction of V^{5+} to V^{4+} to enable the intercalation of Li into the layered structure of V_2O_5. As a result, a mixture of α+ε-$Li_xV_2O_5$ phases are formed as indicated in Eq. (2) [6,24,25]. The structures of these phases do not differ much from the layered structure of V_2O_5, as shown in Fig. 2b. Upon further discharge, two stable plateaus at 2.27 and 2.07 V are observed, which is related to the reduction peaks in the CV at 2.22 V and 2.11 V. The plateau at 2.27 V is an indication of the formation of δ-$Li_xV_2O_5$, as V^{4+} is partially reduced to V^{3+}, forming the mixed phase of δ- and γ-$Li_xV_2O_5$. In contrast to α, ε and δ phases, the γ phase has distorted layers of VO_5 octahedra (Fig. 2b). At the 2.07 V plateau, we believe that formation of δ-$Li_xV_2O_5$ to γ-$Li_xV_2O_5$ has occurred. Further discharge to 1.75 V causes the irreversible formation of γ-$Li_xV_2O_5$, reducing the cyclic retention capabilities of the VNF. This is consistent with the reduction peak at 1.95 V as seen in the CV.

In subsequent charge–discharge cycles (Fig. 6a), the plateaus are not prominent, indicating the Li^+ intercalation/de-intercalation processes occurred reversibly in the mixed phases of $Li_xV_2O_5$ formed after the first discharge. Specific capacity of 300 mAh g^{-1} can be obtained from the first discharge and increased to 316 mAh g^{-1} in the second discharge cycle. The cyclic retention was 70% after 20 cycles and 50% after 50 cycles. The columbic efficiency (Fig. 6c inset) of the VNF cell is maintained at nearly 100% for all the cycles.

The VNF cell is also cycled at 0.1 C rate in a cathodic voltage range of 2.0–4.0 V vs. Li/Li^+ (Fig. 6b). Similar to the first charge–discharge cycle in Fig. 6a, there was the presence of three prominent plateaus at 3.20, 2.27 and 2.07 V respectively, however, at the last plateau (2.07 V), the phase transformation is reduced, as discharging is not carried out below 2.0 V vs. Li/Li^+. The fourth discharge plateau due to discharging below 2.0 V is also not present. In comparing the second discharge cycles in Figs. 6a and 5b, it is observed that the second discharge cycle in

Fig. 6b still had the presence of multiple plateaus, as compared to that in Fig. 6a, which had no plateaus. This is an indication that irreversible phase transformation of δ-$Li_xV_2O_5$ to γ-$Li_xV_2O_5$ is reduced by using a cathodic voltage range. This leads to an improved cyclic retention of the VNF cells, as compared to the lithium cell cycled from 1.75 to 4.0 V (Fig. 6c). It is possible that the cyclic retention of VNF is improved by preventing the formation of the γ-$Li_xV_2O_5$ phase, which has a distorted crystal structure (Fig. 2b). This data is in agreement with that mentioned by Mai et al. [16] in which an irreversible phase transition occurred at 1.9 V. Specific capacity of 230 mAh g^{-1} is achieved in the first discharge cycle, which is increased to 310 mAh g^{-1} in the second discharge cycle. Due to the reduction in extent of irreversible phase transformations, the cyclic retention of the cell cycled within the range 2.0–4.0 V was 74% after 50 cycles. This cell shows a large improvement, as compared that of the cell cycled within the full range of 1.75–4.0 V, for which the cyclic retention is 50% after cycling for 50 cycles at 0.1 C rate. The columbic efficiency (Fig. 6c inset) of this VNF cell is also maintained at nearly 100% for all the 50 cycles.

Cycling of the VNF cells at varying constant C-rates is carried out (Fig. 6d) between 1.75 and 4.0 V. Changes in C-rate (i.e. current density) resulted in stepwise dependence of the specific capacity on cycle number. The capacity decreases slowly at 0.1 C for prolonged cycling but reduced significantly when the C-rate is increased to 1 C. While the capacity is reduced at higher C-rates, the cyclic retention is still maintained. Upon increasing the cycling rate from 0.1 to 1 C, the specific capacity decreases from 200 to 160 mAh g^{-1}, but the cyclic retention is maintained at 70% after cycling for 20 cycles at 1 C rate. When the cycling rate is returned to 0.1 C, the capacity is recovered, increasing from 110 to 160 mAh g^{-1}.

In another VNF cell (Fig. 6d inset), different current rates, namely 0.1, 0.2, 0.5, 1 and 1.5 C are applied to ensure the capacity retention. As the C-rate is increased from 0.1 to 0.2 C, the decrease in specific capacity is small (from 179 to 168 mAh g^{-1}). Further increase of the C-rate to 0.5 C only reduced the capacity from 126 mAh g^{-1} (after 10 cycles at 0.2 C rate) to 110mAhg^{-1}. After cycling for 10 cycles at 0.5 C rate, the cell is cycled at 1 C rate, in which 88% of the capacity was retained. When the C rate is

increased from 1 to 1.5 C, the specific capacity does not decrease much, retaining 96% of the capacity. Upon returning the cell to cycling at 0.1 C rate, the capacity recovers to 110 mAh g^{-1} and is subsequently maintained at 130 mAh g^{-1} for at least the next 10 cycles. It can be concluded that the VNF cells show good rate capabilities as the capacity retention is maintained despite cycling at higher C rates.

Electrochemical impedance spectra (EIS) for coin-cells with electrospun VNF are recorded in the frequency range 100 kHz to 10 mHz. Nyquist ($-Z''$ vs. Z') plots after stabilizing the fresh cell and after 10 cycles are shown in Fig. 7a. The cells display two partially overlapped semicircles in the low and middle frequency range and a straight line in the low-frequency range, suggesting VNF electrode kinetics [24]. For the fresh cell, the Nyquist plots consist of three parts, a high-to-middle frequency semicircle between 100 kHz and 10 Hz, another semicircle at the low-frequency (5–0.25 Hz) and a sloping line with a phase angle of about 45° to the real axis (Z') in the lower frequency range (<0.1 Hz), corresponds to Warburg-type element. The ionic diffusion from the bulk of electrolyte to the reaction sites affects impedance mostly at high frequencies. According to the literature [26,27], the high-to-middle frequency semicircle is related to the lithium-ions migration through the solid electrolyte interphase (SEI) layer and surface film capacitance, another semicircle at the low-frequency is related to lithium ion (charge) transfer as well as on the lithium ion concentration in an electrolyte and interfacial capacitance between VNF/electrolyte interface. The sloping straight line at very low frequency corresponds to the dominant mass transport and is indicative of controlled diffusion of electroactive species across the interface between surface films in the VNF matrix; it also involves the capacitive effect of the conducting carbon.

To perform a quantitative analysis, a simple equivalent circuit is configured to simulate the EIS, shown in Fig. 7b and circuit parameters are calculated by using the series combination of R_s, R_{SEI+ct}//CPE_{SEI+dl}, R_b//CPE_b and Wo, the finite length Warburg resistance (open-circuit terminus). At high characteristic frequency, intercept of the semicircle extended to the Z' axis is reflected by an ohmic resistance (R_s), which includes ionic resistance from the separator and resistance of the electrolyte. R_{SEI+}ct is ascribed to

resistance due to the lithium ion migration through the interface between the surface layer of the VNF electrode/electrolyte and surface film resistance. CPE_{SEI+dl} corresponds to the surface film and double-layer capacitance at the porous VNF electrode surface. The bulk resistance (R_b) arises due to combination of electronic resistivity of active material (VNF) and ionic conductivity of electrolyte filled by the pores of the composite electrode (active material, conducting carbon and binder). The constant phase element CPE_b is the bulk capacitance arising due to the complicated electrochemical processes. The constant phase element is an empirical impedance function of the type, $CPE_{SEI+dl/b} = A(j\omega)^{-\alpha\ SEI+dl/b}$, replaced with capacitance by taking into account the rough nature of the electrode, where ω is the angular frequency, and A and $\alpha_{dl/b}$ are the constants. The degree of distortion of the impedance spectra can be obtained from the value of $\alpha_{SEI+dl/b}$ [28,29].

The experimental data are subjected to a nonlinear least square fitting procedure and equivalent circuit parameters are obtained for VNF fresh cell and after cycling. The semicircles with a characteristic frequency of 63 Hz and 1 Hz before cycling and a single semicircle at 31 Hz after cycling evaluate degree of intercalation and deintercalation of lithium ions at VNF electrode/electrolyte interface. Cells, before and after cycling, show almost constant value of ohmic resistance, $R_s \sim 2.84\Omega$ arising mainly from the resistance of electrolyte. R_{SEI+}ct is observed to decrease from 485 to 37 Ω for VNF. The contribution due to SEI formation is negligible in the case of freshly made cell. After cycling, the decrease in impedance observed for VNF, indicates the evidence of SEI formation in the higher frequency region, overlapped with the bulk resistance region. The presence of two semicircles is clearly apparent in the phase angle vs. log frequency (shown in Fig. 7c) of the cycled cell. It is expected that during long-term cycling, the surface reactions at electrolyte/electrode interface can also lead to the worsening of the electrochemical properties of active electrode materials, forming insoluble products (mixture of $Li_xV_2O_5$ phases) which exhaust Li^+ content in electrodes, blocking the pores of the electrodes, resulting in the increased charge transfer impedance [30]. The capacitance CPE_{SEI+dl} is also observed to decrease during cycling from 8.88 to 4.02 μF for VNF electrode. This slight decrease for VNF can be ascribed to the available electroactive surface area facilitated by VNF matrix through which charge transfer occurs. During every discharge process, the

thickness of double layer decreases along with the active charge-transfer processes (or Li^+ transfer in the VNF matrix). When the CPE_{dl} reaches the maximum value, the vacancies of VNF are fully occupied by Li^+. The further transformation to $Li_xV_2O_5$ phases gives rise to the rebuilding of new capacitive double layer. This process repeats until the VNF electrode reaches to the full discharged state [31]. The significant increase in bulk resistance from 483.9 to 1173 Ω after cycling is observed. Therefore, it is expected that an increase in bulk resistance to electron or ion transfer will result in slow kinetics, large activation polarizations and leads to a significant loss of cycling efficiency and capacity fading. The Warburg diffusion resistance Wo increased from 0.19 to 103 mΩ after cycling thus showed decrease in the low frequency bulk capacitance CPE_b from 0.55 to 0.02 mF. This rather high capacitance before cycling could be due to the accumulating of charge before the Faradic reaction takes place. After cycling, the change in bulk structure and cathode surface has reduced the amount of diffusion pathways, and decreases the utilization of active materials thus increasing Warburg resistance for VNF. Therefore VNF, having porous interconnected morphology, are considered to have potential in minimizing diffusion barriers, and ionic and electronic resistances to decrease the internal resistance as well as to facilitate electrolyte accessibility in the cathode network.

As clearly seen, Nyquist plots of VNF has a much larger diffusivity constant, as shown by the Warburg element. This indicates that more lithium ions are entering the nanofibrous structure of VNF, which is contributed by the electrospinning method of synthesis. The porous, randomly interconnected network of VNF gives rise to a large surface area, which allows increased contact of the electrolyte and the electrode material, and facilitates the movement of lithium ions into and from the VNF cathode.

4. CONCLUSION

Single phase, one-dimensional V_2O_5 polycrystalline nanofibers (VNF) of high aspect ratio are synthesized via electrospinning. Inter-comparison of FESEM and TEM data show a transition from smooth, amorphous as-spun nanofibers to interconnected, porous and polycrystalline V_2O_5 nanofibers after sintering, with good agreement of crystal sizes as

shown in XRD. FTIR studies show the complete removal of polymeric precursors via the sintering step. Electrochemical tests indicate that an electrode composed of electrospun VNF exhibited initial discharge capacity of 320 mAh g^{-1} and excellent coulombic efficiency (~100%) is maintained throughout 50 charge–discharge cycles. Through the lithium intercalation/deintercalation process, the V_2O_5 phase is converted to a mixture of $Li_xV_2O_5$ phases, as explained via cyclic voltammetry and galvanostatic charge–discharge cycling. When applied in the cathodic range (2.0–4.0 V vs. Li/Li^+), the cyclic retention of VNF is improved from 50 to 74% by the prevention of irreversible phase transformations. The interconnected nanofibrous VNF network also enables good rate capabilities. Electrochemical impedance studies carried out before and after cycling bring about new insights to the kinetics of VNF during the electrochemical processes and provided explanation for the cyclic retention properties of V_2O_5 during the Li intercalation/de-intercalation processes, in general. More importantly, these studies prove the increase of available electroactive surface area created by the electrospun network in VNF, improving the accessibility of electrolyte to the cathode material and also increasing the overall efficiency of the Li-ion half-cells made using such electrodes.

5. ACKNOWLEDGEMENTS

This work was supported by funding from the National Research Foundation, Clean Energy Research Project grant number NRF2009EWT-CERP001-036 and L'Oreal-UNESCO Singapore for Women in Science fellowship (2010). Authors also acknowledge Timcal Ltd. (www.timcal.com) for providing gratis Super P™ Li Carbon black.

REFERENCES

[1] D. Liu, Y. Liu, B.B. Garcia, Q. Zhang, A. Pan, Y.-H.Jeong, G. Cao, J. Mater. Chem. 19 (2009) 8789–8795.

[2] T. Zhai, H. Liu, H. Li, X. Fang, M. Liao, L. Li, H. Zhou, Y. Koide, Y. Bando, D. Golberg, Adv. Mater. 22 (2010) 2547–2552.

[3] F. Cheng, J. Chen, J. Mater. Res. 21 (2006) 2744–2757.

[4] C. Ban, N.A. Chernova, M.S. Whittingham, Electrochem. Commun. 11 (2009) 522–525.

[5] C. Ban, M.S. Whittingham, Solid State Ionics 179 (2008) 1721–1724.

[6] A.M. Glushenkov, M.F. Hassan, V.I. Stukachev, Z. Guo, H.K. Liu, G.G. kushinov, Y. Chen, J. Solid State Electrochem. 14 (2010) 1841–1846.

[7] C. Xiong, A.E. Aliev, B. Gnade, K.J. Balkus Jr., Am. Chem. Soc. Nano 2 (2008) 293–301.

[8] C.V.S. Reddy, J. Wei, Z. Quan-Yao, D. Zhi-Rong, C. Wen, S.-i. Mho, R.R. Kalluru, J. Power Sources 166 (2007) 244–249.

[9] X. Ren, Y. Jiang, P. Zhang, J. Liu, Q. Zhang, J. Sol-Gel Sci. Technol. 51 (2009) 133–138.

[10] F. Huguenin, E.M. Girotto, R.M. Torresi, D.A. Buttry, J. Electroanal. Chem. 536 (2002) 37–45.

[11] M.J. Parent, S. Passerini, B.B. Owens, W.H. Smyrl, J. Electrochem. Soc. 146 (1999) 1346–1350.

[12] E.A. Ponzio, T.M. Benedetti, R.M. Torresi, Electrochim. Acta 52 (2007) 4419–4427.

[13] M. Macias, A. Chacko, J.P. Ferraris, K.J. Balkus Jr., Micropor. Mesopor. Mater. 86 (2005) 1–13.

[14] W.E. Teo, S. Ramakrishna, Nanotechnology 17 (2006) R89–R106.

[15] V. Thavasi, G. Singh, S. Ramakrishna, Energy Environ. Sci. 1 (2008) 205–221.

[16] L. Mai, L. Xu, C. Han, X. Yu, Y. Luo, S. Zhao, Y. Zhao, Nano Lett. 10 (2010) 4750–4755.

[17] G. Wee, H.Z. Soh, Y.L. Cheah, S.G. Mhaisalkar, M. Srinivasan, J. Mater. Chem. 20 (2010) 1–7.

[18] H.M. Rietveld, Acta Crystallogr. 22 (1967) 157.

[19] H.M. Rietveld, J. Appl. Crytallogr. 2 (1969) 65.

[20] R.W. Cheary, A. Coelho, J. Appl. Crystallogr. 25 (1992) 109.

[21] Y.-Q. Chu, Q.-Z. Qin, Chem. Mater. 14 (2002) 3152–3157.

[22] C. Navone, R. Baddour-Hadjean, J.P. Pereira-Ramos, R. Salot, Electrochim. Acta 53 (2008) 3329–3336.

[23] K.H. Kim, D.K. Roh, I.K. Song, B.C. Lee, S.H. Baeck, J. Solid State Electrochem. 14 (2010) 1801–1805.

[24] C.V.S. Reddy, A.-P.Jin, X. Han, Q.-Y. Zhu, L.-Q. Mai, W. Chen, Electrochem. Commun. 8 (2006) 279–283.

[25] J.M. Cocciantelli, J.P. Doumerc, M. Pouchard, M. Broussely, J. Labat, J. Power Sources 34 (1991) 103–111.

[26] K.M. Shaju, G.V. Subba Rao, B.V.R. Chowdari, Electrochim. Acta 49 (2004) 1565.

[27] S.S. Zhang, K. Xu, T.R. Jow, Electrochim. Acta 49 (2004) 1057.

[28] C.-j. Cui, G.-m. Wu, B.Z. Jun Shen, Z.-h. Zhang, H.-y. Yang, S.-f. She, Electrochim. Acta 55 (2010) 2536–2541.

[29] S.-I. Pyun, J.-S. Bae, Electrochim. Acta 41 (1996) 919–925.

[30] D.A. Semenenko, A.M.S.T.L. Kulova, D.M. Itkis, E.A. Pomerantseva, E.A. Goodilin, Y.D. Tretyakov, Mendeleev Commun. 20 (2010) 12–14.

[31] Q.-C. Zhuang, T.Wei, L.-L.Du,Y.-L.Cui, L.Fang, S.-G.Sun, J.Phys.Chem. C 114 (2010) 8614–8621.

List of Figures

data. Symbols present experimental spectra and continuous lines represent fitted data using equivalent electrical circuit.

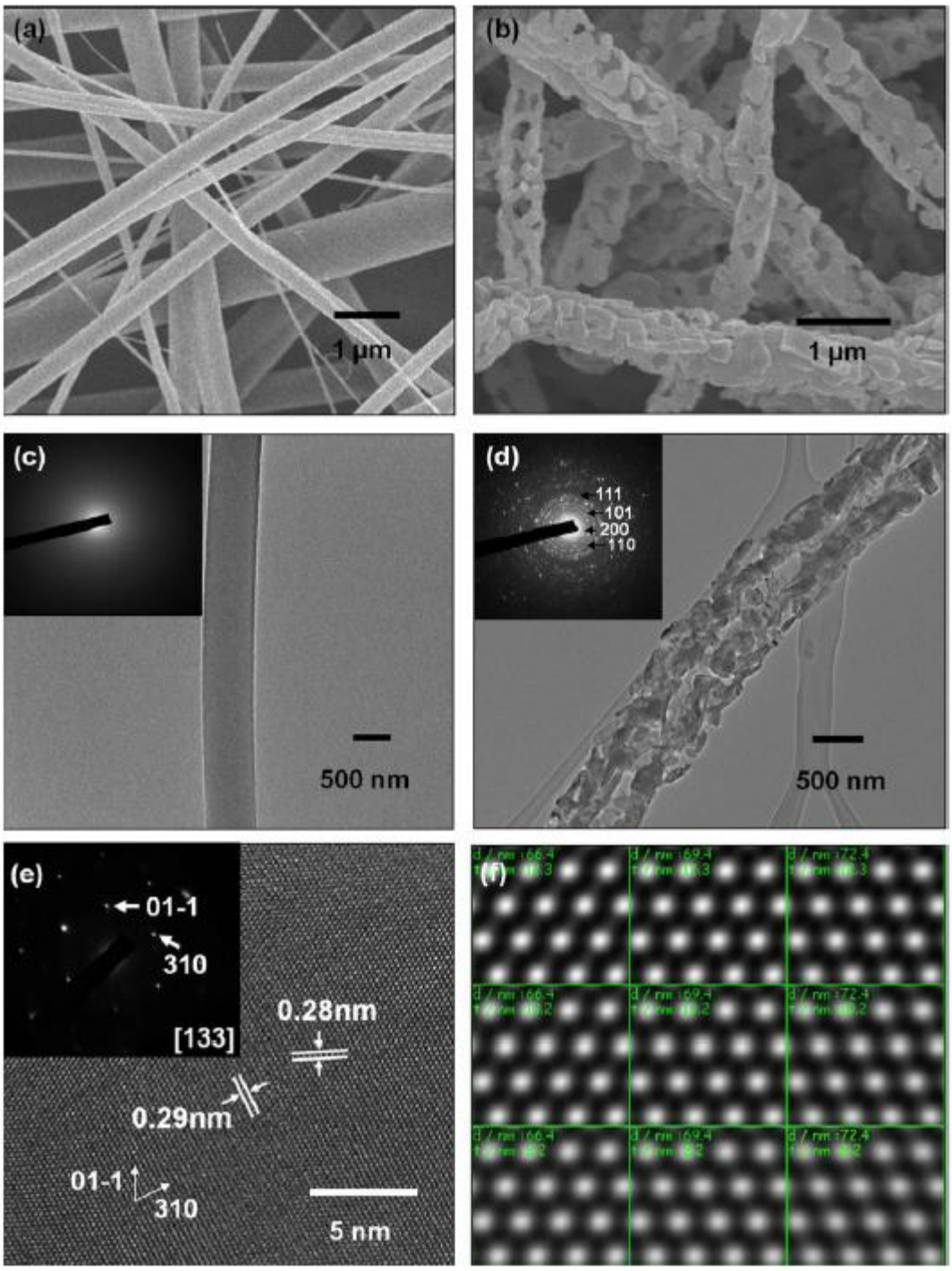
(a)
1 μm
(b)
1 μm
(c)
500 nm
(d)
111
101
200
110
500 nm
(e)
01-1
310
[133]
0.28nm
0.29nm
01-1
310
5 nm
(f)

Figure 1

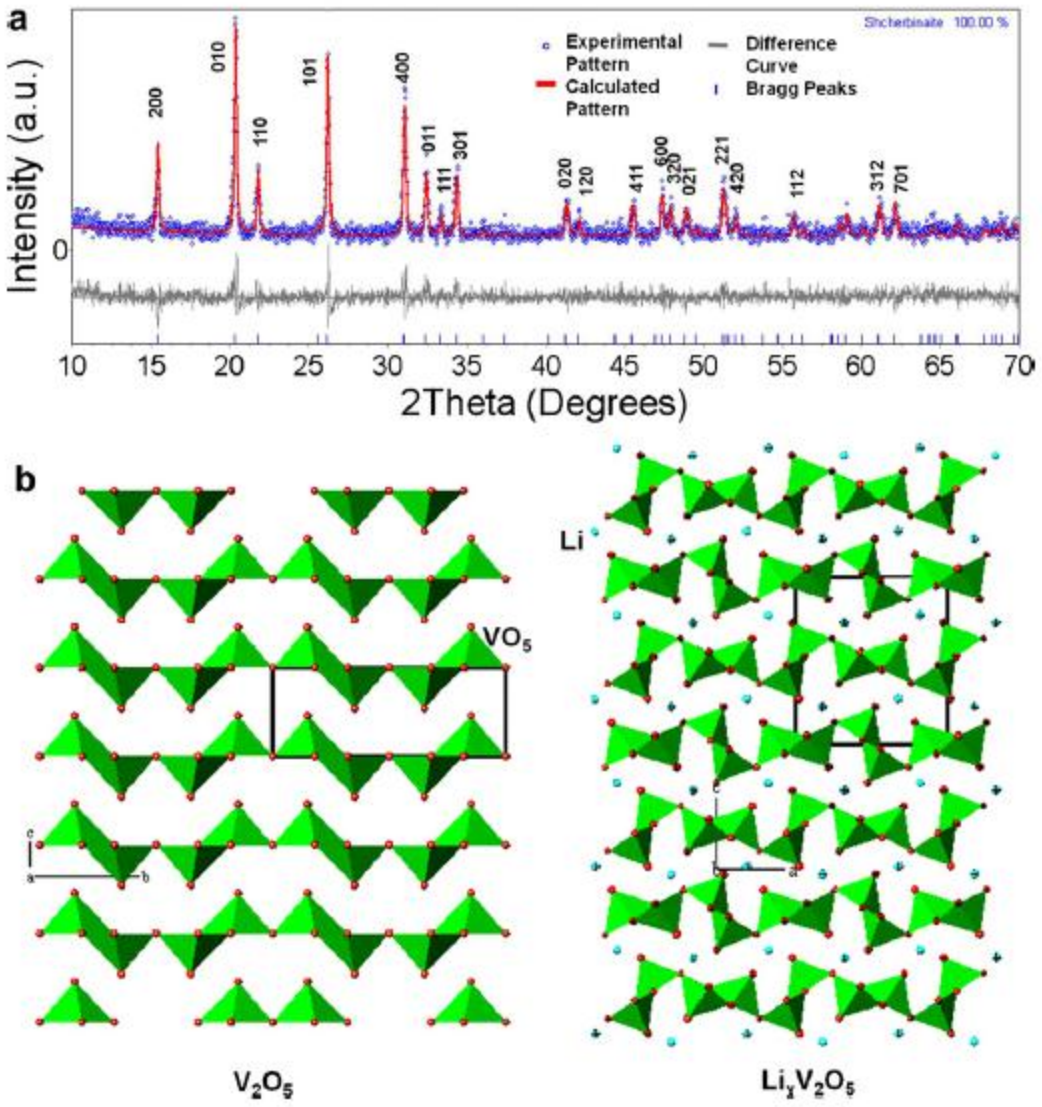
a
Intensity (a.u.)
0
2Theta (Degrees)
10 15 20 25 30 35 40 45 50 55 60 65 70
Experimental Pattern
Calculated Pattern
Difference Curve
Bragg Peaks
200
010
110
101
400
011
111
301
020
120
411
600
320
021
221
420
112
312
701
b
VO5
Li
V2O5
LiyV2O5

Figure 2

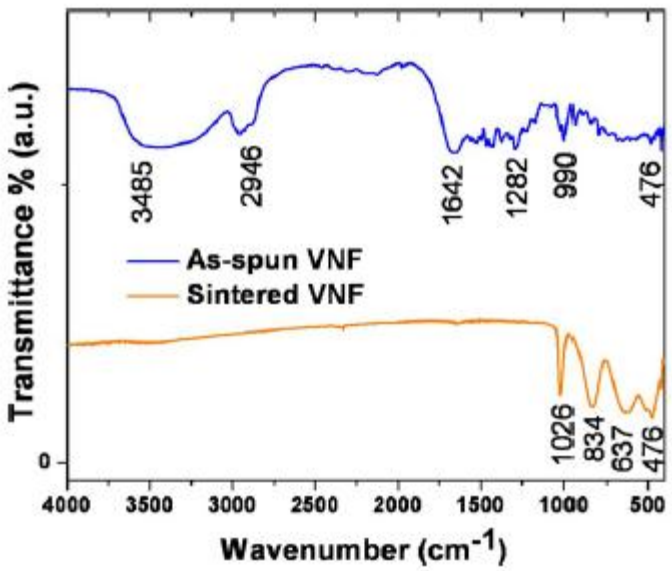
Transmittance % (a.u.)
0
3485
2946
1642
1282
990
476
As-spun VNF
Sintered VNF
1026
834
637
476
4000
3500
3000
2500
2000
1500
1000
500
Wavenumber (cm-1)

Figure 3

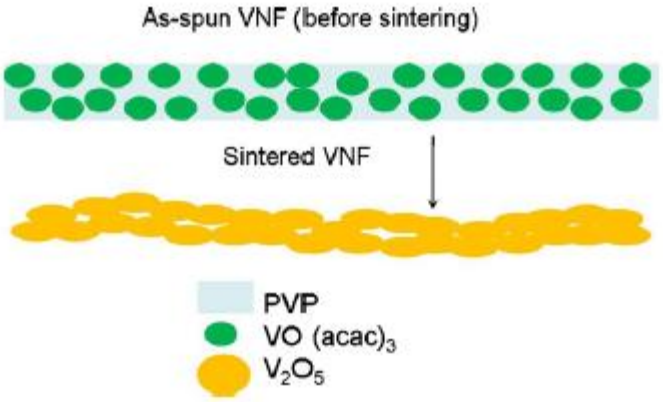

Figure 4

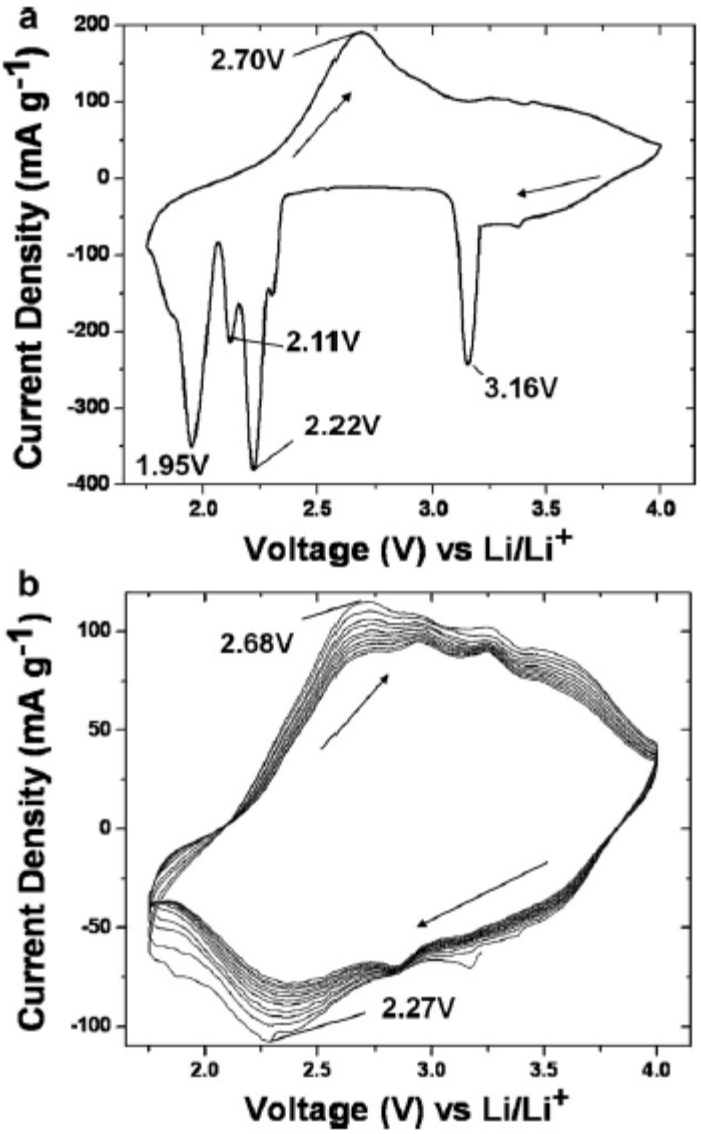
a
Current Density (mA g-1)
2.70V
2.11V
3.16V
2.22V
1.95V
Voltage (V) vs Li/Li+
b
Current Density (mA g-1)
2.68V
2.27V
Voltage (V) vs Li/Li+

Figure 5

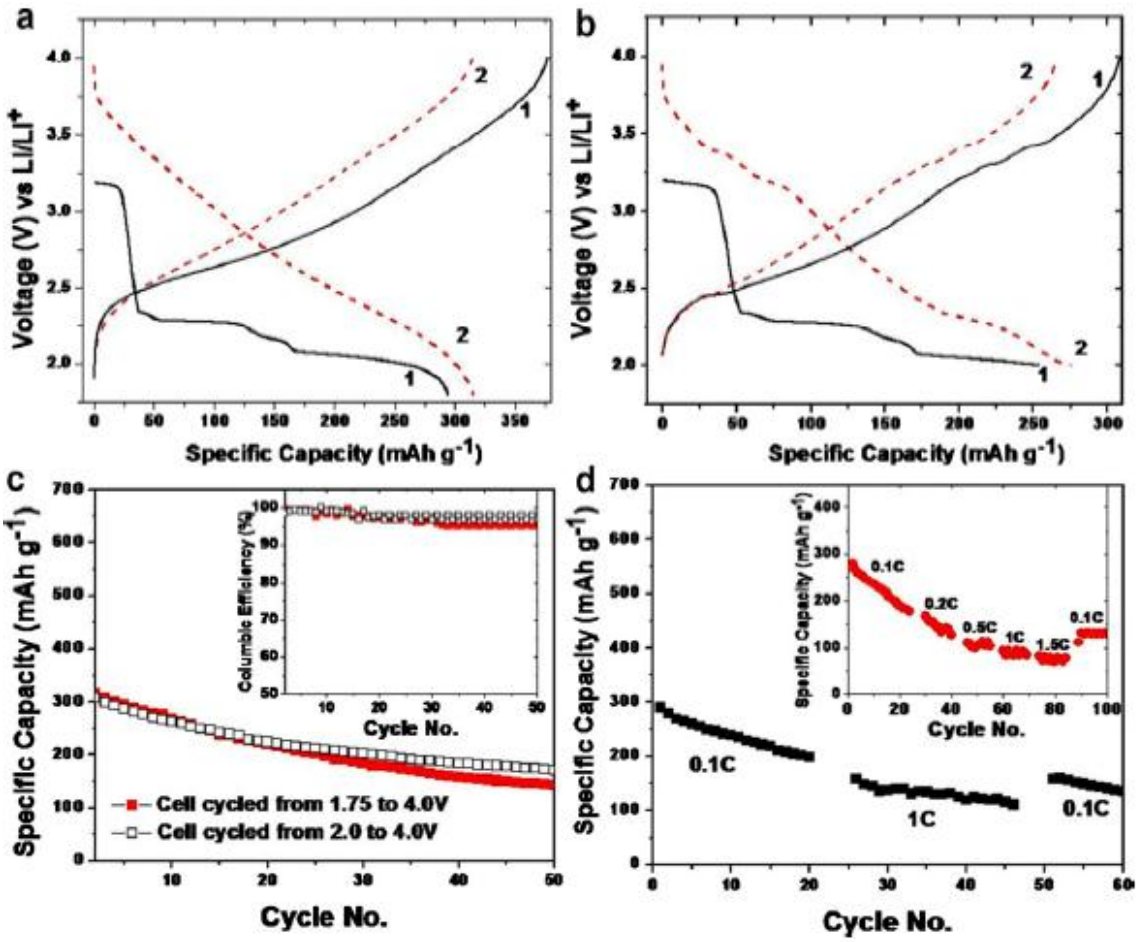
a
b
c
d
Voltage (V) vs LI/LI+
Specific Capacity (mAh g-1)
Specific Capacity (mAh g-1)
Cycle No.
Columbic Efficiency (%)
Cell cycled from 1.75 to 4.0V
Cell cycled from 2.0 to 4.0V
0.1C
0.2C
0.5C
1C
1.5C
0.1C
1C
0.1C

Figure 6

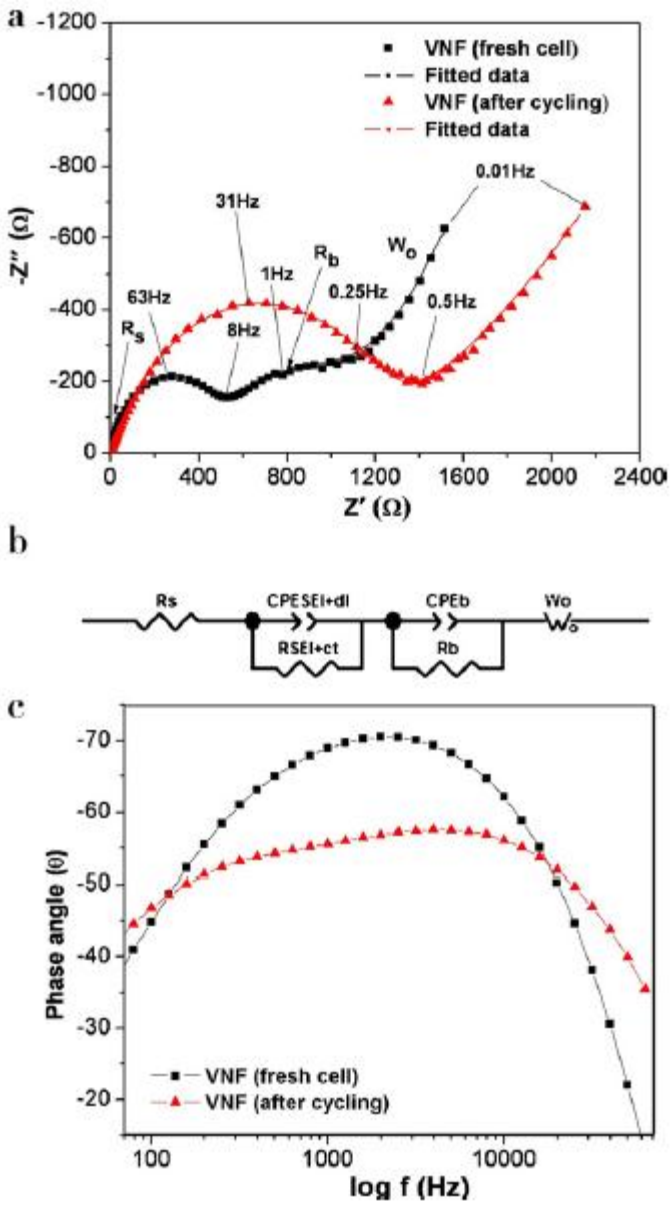
a
-1200
-1000
-800
-600
-400
-200
0
-Z'' (Ω)
0
400
800
1200
1600
2000
2400
Z' (Ω)
VNF (fresh cell)
Fitted data
VNF (after cycling)
Fitted data
0.01Hz
31Hz
Rb
Wo
1Hz
63Hz
0.25Hz
0.5Hz
Rs
8Hz
b
Rs
CPESEI+dl
CPEb
Wo
RSEI+ct
Rb
c
-70
-60
-50
-40
-30
-20
Phase angle (θ)
100
1000
10000
log f (Hz)
VNF (fresh cell)
VNF (after cycling)

Figure 7